

**Electrodynamics in the near-field regions of anisotropic nanoscopic films and platelets**B. I. Lembrikov,<sup>1,2</sup> M. A. Itskovsky,<sup>1</sup> H. Cohen,<sup>2</sup> and T. Maniv<sup>1</sup><sup>1</sup>*Chemistry Department, Technion, Haifa 32000, Israel*<sup>2</sup>*Weizmann Institute of Science, Rehovot 76100, Israel*<sup>3</sup>*Holon Academic Institute of Technology, Golomb 52, Holon 58102, Israel*

(Received 19 September 2002; published 4 February 2003)

An electromagnetic theory of valence electron excitations by an external electron beam in the near field regions of uniaxial anisotropic nanoplatelets is presented. It is shown that in an interface of high symmetry (i.e., perpendicular to the symmetry axis) only extraordinary waves can be excited by the electron beam, usually as surface-plasmon-polariton modes. However, the anisotropy also allows excited extraordinary waves to propagate as waveguide modes. In an interface of low symmetry a mixture of both waves is inseparably excited. Application is made to directional near-field electron energy loss spectroscopy of uniaxial dielectric nanoplatelets. It is found that all relevant length parameters in this spectroscopy happen to fall in the same range, giving rise to enhanced sensitivity of the electron energy loss (EEL) signal to the size and geometry of the detected nanoparticle. The breakdown of momentum conservation in the electron-plasmon scattering event, associated with the finite size of the platelet along the beam direction, strongly changes the EEL signal pattern.

DOI: 10.1103/PhysRevB.67.085401

PACS number(s): 78.67.Ch, 82.80.Pv, 07.79.Fc

**I. INTRODUCTION**

The electronic properties of conducting and semiconducting materials with restricted dimensions on a nanometer length scale have attracted much attention recently. Various spectroscopical techniques for investigating the electronic structure of these materials have been developed. In particular, the excitation of electromagnetic (EM) waves in crystalline nanoparticles by external high energy electron beams ( $e$  beams) have been exploited to study unique aspects of the valence electron properties in these nanostructures.<sup>1-4</sup>

In a special configuration available in scanning transmission electron microscopes (STEM), where the  $e$  beam is restricted to the vacuum surrounding a selected nanoparticle,<sup>3</sup> the beam-particle interaction is determined by those modes, which generate nonvanishing electric fields outside the particle boundaries. The dominant coupling in the near-field regions is, therefore, with nonradiative collective oscillations such as surface plasmons, surface plasmon-polaritons (SPPs) or wave-guide modes.<sup>5</sup> With beam electrons of relativistic velocity, i.e.,  $v \sim 0.5c$ , typical to these microscopes, the characteristic wavelength,  $\lambda \sim v/\omega$ , of an EM excitation with frequency  $\omega$  is in the range of 10 nm, where the SPP modes have a strong spatial dispersion. As shown below, this unique feature of the spectroscopical technique under consideration enables a very sensitive detection of geometrical and size effects of the nanocrystal via selection of impact parameter and beam-object orientation.

The problem of collective EM excitations in anisotropic media with restricted dimensions is of general interest. A comprehensive study of surface plasmons propagating at the boundary of a semi-infinite isotropic dielectric medium and in a thin isotropic film was carried out by Raether.<sup>5,6</sup> An adequate theoretical description of surface plasmon excitations in a nanoplatelet, taking into account retardation effects, material anisotropy, and the platelet finite dimensions, requires a solution of Maxwell equations for an anisotropic medium with the account of the corresponding boundary

conditions and the external current distribution. In the general case, this is a very complicated mathematical problem due to the boundary conditions on surface intersections, and to the asymmetry between the various surfaces, dictated by the anisotropy of the medium, the latter giving rise, for example, to the existence of ordinary and extraordinary waves in a uniaxial symmetry.<sup>7</sup> To our best knowledge, such a comprehensive electrodynamic theory of the surface collective modes has not been published yet. Lucas *et al.*<sup>8</sup> presented a dielectric model for calculating the electron energy loss spectra of multishell fullerenes. This work focused on geometrical and size effects, neglecting, however, dielectric anisotropy and retardation effects. A more recent work<sup>9</sup> investigated nonradiative SPP in metal-cladded isotropic dielectric cylinders, using fully retarded calculations. Some relevant theoretical considerations can also be found in recent experimental papers published by the Orsay group and collaborators,<sup>10-13</sup> who focused mainly on probing radial and tangential plasmon modes in layered nanospheres and nanotubes by near-field electron-energy loss spectroscopy.<sup>3</sup> However, their theoretical approach neglected EM retardation and quantum effects.

In the present paper we develop a theory for EM surface and wave-guide modes in an anisotropic (uniaxial) dielectric film. The EM theory is applied to the calculation of the electron energy loss (EEL) function of nanoplatelets in the near-field configuration, at two different orientations of the  $e$  beam with respect to the nanoparticle (see Fig. 1,  $z$  and  $y_n$  scans).

We find that under certain conditions the dielectric anisotropy introduces additional energy gaps into the SPPs band structure. In these energy gaps SPPs transform into guided modes. The unique feature of these modes is that, unlike the ordinary wave-guide modes existing in isotropic films, they have a longitudinal electric field component, which allows coupling with an external  $e$  beam. These anisotropy-induced excitations tend, however, to wash out upon introduction of realistic damping parameters. On the other hand, a strong

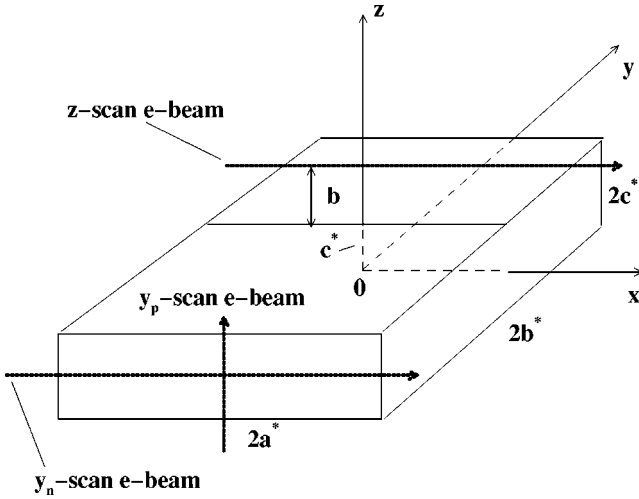


FIG. 1. A schematic illustration of various beam configurations relative to a rectangular uniaxial anisotropic platelet ( $e$ -beam directions are indicated by the bold arrows).  $z$  scan: the  $e$  beam is above a surface normal to the symmetry  $z$  axis.  $y_n$  and  $y_p$  scans: the  $e$  beam is above a surface normal to the  $y$  axis, and normal ( $n$ ) or parallel ( $p$ ) to the symmetry  $z$  axis, respectively. The platelet dimensions are  $2a^* \times 2b^* \times 2c^*$ .  $b$  is the distance between the  $e$  beam path and the surface (the impact parameter).

sensitivity of the near-field spectroscopy to size and geometrical effects is found when the impact parameter approaches the corresponding particle dimensions and both are comparable with the inverse momentum transfer between the beam electron and the SPP.

The paper is organized as follows. The general formalism is presented in Sec. II. In Sec. III we analyze the surface EM normal modes of an anisotropic dielectric film by solving the homogeneous parts of the corresponding Maxwell's equations. In Sec. IV the dielectric tensor is calculated in the framework of the electronic shell model, and the dispersion relations of the various SPP modes are derived. In Sec. V the inhomogeneous boundary problem is solved for two distinct configurations of the external narrow  $e$  beam with respect to the anisotropic dielectric film. In both cases field amplitudes are calculated and analytical expressions for the electron energy loss function are obtained. A comparison of the theory with experimental data taken for MoS<sub>2</sub> nanoplatelets is also presented in Sec. V.

## II. GENERAL FORMALISM

Consider the response of a dielectric film to an external high frequency EM field. The bulk crystal is described by a uniaxial dielectric tensor  $\varepsilon_{ik}(\omega)$ , written in the principal axes  $x, y$ , and  $z$  as

$$\begin{aligned} \varepsilon_{xx} = \varepsilon_{yy} \equiv \varepsilon_{\perp}(\omega) &= \text{Re } \varepsilon_{\perp}(\omega) + i \text{Im } \varepsilon_{\perp}(\omega), \\ \varepsilon_{zz} \equiv \varepsilon_{\parallel}(\omega) &= \text{Re } \varepsilon_{\parallel}(\omega) + i \text{Im } \varepsilon_{\parallel}(\omega). \end{aligned} \quad (1)$$

Two different film orientations are distinguished by the medium symmetry axis, namely the  $z$  axis (see Fig. 1): in the first the film is bounded by the planes  $z = \pm c^*$ , perpendicu-

lar to symmetry axis, while in the second case the film faces are parallel to  $z$ , e.g., at  $y = \pm b^*$ . The external charge and current distributions,  $\rho(\mathbf{r}, t)$  and  $\mathbf{j}(\mathbf{r}, t)$ , respectively, which generate the EM field, are assumed to vanish inside the film, so that the fields can be described by the inhomogeneous macroscopic Maxwell equations

$$\text{curl} \mathbf{E}(\mathbf{r}, t) = -\mu_0 \frac{\partial \mathbf{H}(\mathbf{r}, t)}{\partial t}, \quad (2)$$

$$\text{curl} \mathbf{H}(\mathbf{r}, t) = \mathbf{j}(\mathbf{r}, t) + \frac{\partial \mathbf{D}(\mathbf{r}, t)}{\partial t}, \quad (3)$$

$$\text{div} \mathbf{D}(\mathbf{r}, t) = \rho(\mathbf{r}, t), \quad (4)$$

$$\text{div} \mathbf{H}(\mathbf{r}, t) = 0, \quad (5)$$

with the appropriate boundary conditions at the film surfaces  $z = \pm c^*$  (or  $y = \pm b^*$ ). Here  $\mathbf{E}(\mathbf{r}, t), \mathbf{H}(\mathbf{r}, t), \mathbf{D}(\mathbf{r}, t)$  are the vectors of the electric, magnetic and electric induction fields, respectively. We assume the film to be nonmagnetic, so that the magnetic induction can be written as  $\mathbf{B} = \mu_0 \mathbf{H}$ .

In the linear response approximation the time Fourier transforms of the electric induction and the corresponding electric field with frequency  $\omega$  are connected by the material equations inside the anisotropic crystalline film,

$$D_i(\mathbf{r}, \omega) = \varepsilon_0 \varepsilon_{ik}(\omega) E_k(\mathbf{r}, \omega), \quad (6)$$

whereas outside the film (which is assumed to be a free space)

$$\mathbf{D}^{out}(\mathbf{r}, \omega) = \varepsilon_0 \mathbf{E}^{out}(\mathbf{r}, \omega). \quad (7)$$

The solution of Maxwell equations outside the film can be facilitated by using the Hertz vector formalism.<sup>14-16</sup> The Hertz vector  $\mathbf{\Pi}(\mathbf{r}, \omega)$ , outside the film satisfies the equation<sup>14</sup>

$$\nabla^2 \mathbf{\Pi}(\mathbf{r}, \omega) + \frac{\omega^2}{c^2} \mathbf{\Pi}(\mathbf{r}, \omega) = \frac{1}{i\omega \varepsilon_0} \mathbf{j}(\mathbf{r}, \omega), \quad (8)$$

so that the corresponding electric and magnetic fields can be written as

$$\mathbf{E}^{out}(\mathbf{r}, \omega) = \text{grad div} \mathbf{\Pi}(\mathbf{r}, \omega) + \frac{\omega^2}{c^2} \mathbf{\Pi}(\mathbf{r}, \omega), \quad (9)$$

$$\mathbf{H}^{out}(\mathbf{r}, \omega) = -i\omega \varepsilon_0 \text{curl} \mathbf{\Pi}(\mathbf{r}, \omega). \quad (10)$$

The electric field inside the anisotropic crystalline film is determined by the wave equations

$$\text{curl curl} \mathbf{E}(\mathbf{r}, \omega) = -\frac{\omega^2}{c^2} \varepsilon_0 \varepsilon_{ik}(\omega) E_k(\mathbf{r}, \omega). \quad (11)$$

For a uniaxial crystal Eq. (11) has two essentially different solutions: an ordinary wave ( $o$  wave), with electric field  $\mathbf{E}^o(\mathbf{r}, \omega)$ , and an extraordinary wave ( $e$  wave), with  $\mathbf{E}^e(\mathbf{r}, \omega)$ .<sup>7</sup> The  $o$  wave is polarized in the plane perpendicular to the symmetry axis, and it is purely transverse, so that

$\text{div}\mathbf{E}^o=0$ . The  $e$  wave satisfies the condition  $\text{div}\mathbf{D}^e=0$  and has a component parallel to the symmetry axis. In the non-relativistic limit  $\omega/c\rightarrow 0$  the  $o$  wave vanishes, while the  $e$  wave reduces to a purely longitudinal one, determined by the equation  $\text{curl}\mathbf{E}^e=0$ . Consequently, the electric and magnetic fields inside the anisotropic film can be written as a superposition of extraordinary and ordinary waves:

$$\mathbf{E}(\mathbf{r},\omega)=\mathbf{E}^e(\mathbf{r},\omega)+\mathbf{E}^o(\mathbf{r},\omega), \quad (12)$$

$$\mathbf{H}(\mathbf{r},\omega)=\mathbf{H}^e(\mathbf{r},\omega)+\mathbf{H}^o(\mathbf{r},\omega). \quad (13)$$

### III. SURFACE PLASMON POLARITON MODES IN A UNIAxIAL ANISOTROPIC DIELECTRIC FILM

In the linear response approximation all EM excitations can be obtained from the homogeneous Maxwell's equations. We first consider the case when the film surfaces are perpendicular to the symmetry axis (the  $z$  axis). In the absence of external current the solution of Eq. (8) can be represented as a Fourier integral:

$$\mathbf{\Pi}(\mathbf{r},\omega)=\int_{-\infty}^{\infty} dk_x \int_{-\infty}^{\infty} dk_y \exp[i(k_x x+k_y y)] \quad (14)$$

$$\times \mathbf{\Pi}(z,k_x,k_y,\omega). \quad (15)$$

In the regions outside the film (at  $z>c^*$  and  $z<-c^*$ ; see Fig. 1),  $\Pi_y(z,k_x,k_y,\omega)=0$ , and the other components have the form

$$\begin{pmatrix} \Pi_x(z,k_x,k_y,\omega) \\ \Pi_z(z,k_x,k_y,\omega) \end{pmatrix} = \begin{pmatrix} A_{+,-} \\ B_{+,-} \end{pmatrix} \exp[\mp \alpha_z(z \mp c^*)], \quad (16)$$

where the extinction coefficient  $\alpha_z$  in the free space is given by

$$\alpha_z = \sqrt{k^2 - \frac{\omega^2}{c^2}}, \quad k^2 \equiv k_x^2 + k_y^2. \quad (17)$$

From Eqs. (9) and (10) we obtain the tangential field components outside the film:

$$E_x^{out} = ik_x \frac{\partial \Pi_z}{\partial z} + \Pi_x \left( \frac{\omega^2}{c^2} - k_x^2 \right), \quad (18)$$

$$E_y^{out} = -k_x k_y \Pi_x + ik_y \frac{\partial \Pi_z}{\partial z}, \quad (19)$$

$$H_x^{out} = \omega \varepsilon_0 k_y \Pi_z, \quad (20)$$

$$H_y^{out} = -\omega \varepsilon_0 k_x \Pi_z - i\omega \varepsilon_0 \frac{\partial \Pi_x}{\partial z}. \quad (21)$$

Inside the film the  $e$  wave has the electric and magnetic field components

$$E_z^e(z,k_x,k_y,\omega) = A^e \exp(q_z^e z) + B^e \exp(-q_z^e z), \quad (22)$$

$$E_x^e = ik_x \frac{\varepsilon_{\parallel}}{k^2 \varepsilon_{\perp}} \frac{\partial E_z^e}{\partial z}, \quad (23)$$

$$E_y^e = ik_y \frac{\varepsilon_{\parallel}}{k^2 \varepsilon_{\perp}} \frac{\partial E_z^e}{\partial z}, \quad (24)$$

$$H_x^e = k_y E_z^e \frac{\omega \varepsilon_0 \varepsilon_{\parallel}}{k^2} E_z^e, \quad (25)$$

$$H_y^e = -k_x \frac{\omega \varepsilon_0 \varepsilon_{\parallel}}{k^2} E_z^e, \quad (26)$$

where

$$q_z^e = \sqrt{\frac{\varepsilon_{\perp}}{\varepsilon_{\parallel}} \left[ k^2 - \frac{\omega^2}{c^2} \varepsilon_{\parallel} \right]}. \quad (27)$$

The  $e$ -wave normal component  $E_z^e$  supports the surface induced charges at  $z = \pm c^*$ .<sup>5</sup> The  $o$  wave is polarized only in the  $xy$  plane (i.e., parallel to the film surface). It has the following field components

$$E_x^o(z,k_x,k_y,\omega) = A^o \exp(q_z^o z) + B^o \exp(-q_z^o z), \quad (28)$$

$$E_y^o = -\frac{k_x}{k_y} E_x^o, \quad (29)$$

$$H_x^o = -i \frac{1}{\omega \mu_0} \frac{k_x}{k_y} \frac{\partial E_x^o}{\partial z}, \quad (30)$$

$$H_y^o = -i \frac{1}{\omega \mu_0} \frac{\partial E_x^o}{\partial z}, \quad (31)$$

where

$$q_z^o = \sqrt{k^2 - \frac{\omega^2}{c^2} \varepsilon_{\perp}}. \quad (32)$$

The continuity of the tangential components  $E_{x,y}$  and  $H_{x,y}$  at the surfaces  $z = \pm c^*$  results in a system of eight equations which has a non-trivial solution for the  $e$  wave and for the  $o$  wave, provided the following conditions are satisfied, respectively:

$$2q_z^e \alpha_z \varepsilon_{\perp} \coth(2q_z^e c^*) + (\alpha_z \varepsilon_{\perp})^2 + (q_z^e)^2 = 0, \quad (33)$$

$$2q_z^o \alpha_z \coth(2q_z^o c^*) + \alpha_z^2 + (q_z^o)^2 = 0. \quad (34)$$

Due to the symmetry of the film (with respect to the central plane  $z=0$ ), these equations can be factorized, e.g., in the case of the  $e$  wave [Eq. (33)], into two independent equations, which determine the dispersion relations of the SPP modes, having either symmetric or antisymmetric field profiles, respectively:

$$\varepsilon_{\perp} \alpha_z + q_z^e \tanh(q_z^e c^*) = 0, \quad (35)$$

$$\varepsilon_{\perp} \alpha_z + q_z^e \coth(q_z^e c^*) = 0. \quad (36)$$

Equation (34) for the  $o$  wave has no real solutions for  $\alpha_z > 0, q_z^o > 0$ , implying that the  $o$  wave is not a surface EM mode. It can propagate, however, within the film as a wave-guide mode, as will be shown below. The various possibilities of wave-guide modes can be examined by allowing  $q_z^o$  and  $q_z^e$  to be purely imaginary, and assuming real dielectric functions [Eqs. (1)]. For an  $o$  wave,  $q_z^o = i|q_z^o|$  under the condition

$$\varepsilon_{\perp} > k^2 c^2 / \omega^2, \quad (37)$$

whereas for an  $e$  wave  $q_z^e = i|q_z^e|$ , provided

$$\varepsilon_{\parallel} > k^2 c^2 / \omega^2, \quad \frac{\varepsilon_{\perp}}{\varepsilon_{\parallel}} > 0 \quad (38)$$

or

$$\varepsilon_{\parallel} < k^2 c^2 / \omega^2, \quad \frac{\varepsilon_{\perp}}{\varepsilon_{\parallel}} < 0. \quad (39)$$

The latter condition corresponds to the strong anisotropy situation, when the dielectric function components  $\varepsilon_{\perp}$  and  $\varepsilon_{\parallel}$  have opposite signs in a certain frequency range.

The dispersion relations (34)–(36) for purely imaginary  $q_z^o$  and  $q_z^e$  reduce to the well-known dispersion relations for symmetric and antisymmetric guided modes.<sup>17</sup> The guided  $o$  wave can exist only for  $\varepsilon_{\perp} > 0$  (see Eq. (37)), whereas the guided  $e$ -wave can exist for both  $\varepsilon_{\perp} > 0$  and  $\varepsilon_{\perp} < 0$ , depending on the sign and magnitude of  $\varepsilon_{\parallel}$ , as seen in Eqs. (38) and (39). The latter property results in a series of alternating energy bands of wave-guide and SPP modes, due to the complicated frequency dependence of the dielectric function [Eq. (1)] (see Sec. IV). In realistic situations the dielectric function in the frequency range of interest here is a complex function, and so any  $e$  wave develops both evanescent and oscillatory fields inside the film, so that the distinction between SPP and guided modes is not very clear.

Now consider the case when the film faces are parallel to the symmetry axis. The electric and magnetic fields  $\mathbf{E}^o$ ,  $\mathbf{E}^e$  and  $\mathbf{H}^o$ ,  $\mathbf{H}^e$ , inside the film,  $|y| < b^*$ , are given, respectively, by

$$E_y^o(y, k_x, k_z, \omega) = A^o \exp(q_y^o y) + B^o \exp(-q_y^o y), \quad (40)$$

$$E_x^o = i \frac{1}{k_x} q_y^o E_y^o, \quad E_z^o = 0, \quad (41)$$

$$H_x^o = -\frac{k_z}{\omega \mu_0} E_y^o, \quad H_y^o = i \frac{k_z}{\omega \mu_0 k_x} \frac{\partial E_y^o}{\partial y}, \quad (42)$$

$$H_z^o = \frac{1}{\omega \mu_0 k_x} \left( \frac{\omega^2}{c^2} \varepsilon_{\perp} - k_z^2 \right) E_y^o \quad (43)$$

and

$$E_z^e(y, k_x, k_z, \omega) = A^e \exp(q_y^e y) + B^e \exp(-q_y^e y), \quad (44)$$

$$E_x^e = \frac{k_x k_z}{k_z^2 - (\omega^2/c^2) \varepsilon_{\perp}} E_z^e, \quad (45)$$

$$E_y^e = -\frac{i k_z}{k_z^2 - (\omega^2/c^2) \varepsilon_{\perp}} \frac{\partial E_z^e}{\partial y}, \quad (46)$$

$$H_x^e = i \frac{\varepsilon_{\perp}}{\omega \mu_0} \frac{(\omega/c)^2}{k_z^2 - (\omega^2/c^2) \varepsilon_{\perp}} \frac{\partial E_z^e}{\partial y}, \quad (47)$$

$$H_y^e = \frac{k_x}{\omega \mu_0} \frac{(\omega/c)^2}{k_z^2 - (\omega^2/c^2) \varepsilon_{\perp}} \varepsilon_{\perp} E_z^e, \quad H_z^e = 0, \quad (48)$$

where

$$q_y^o = \sqrt{k_z^2 + k_x^2 - \frac{\omega^2}{c^2} \varepsilon_{\perp}}, \quad (49)$$

$$q_y^e = \sqrt{\frac{\varepsilon_{\parallel}}{\varepsilon_{\perp}} k_z^2 + k_x^2 - \frac{\omega^2}{c^2} \varepsilon_{\parallel}}. \quad (50)$$

Here, in contrast to the previous case, both  $e$  and  $o$  waves have a component perpendicular to the film faces  $y = \pm b^*$ , and can support surface plasma modes.

The Hertz vector components in the regions  $b^* < y$  and  $y < -b^*$  are given, respectively, by

$$\begin{pmatrix} \Pi_x(y, k_x, k_z, \omega) \\ \Pi_y(y, k_x, k_z, \omega) \end{pmatrix} = \begin{pmatrix} A_{+,-} \\ B_{+,-} \end{pmatrix} \exp[\mp \alpha_y (y \mp b^*)], \quad (51)$$

and  $\Pi_z(z, k_x, k_y, \omega) = 0$ , where

$$\alpha_y = \sqrt{k_x^2 + k_z^2 - \frac{\omega^2}{c^2}}. \quad (52)$$

In the general case the boundary conditions for the electric and magnetic field components  $E_z, D_y = \varepsilon_{\perp} E_y, H_z$  and  $H_y$  at the faces  $y = \pm b^*$  yield a system of eight linear equations, analogous to the eight equations obtained at  $z = \pm c^*$  above. However, here in contrast to the previous case, the  $e$  and  $o$  waves cannot be separated due to symmetry breaking in the  $y$  direction. For this reason, only a mixture of  $e$  and  $o$  surface modes can be excited. An explicit solution, though very complicated, can be derived in such a case. It has a relatively simple form in the limiting case of a semi-infinite sample, with  $b^* \rightarrow \infty$ . The resulting system of four linear homogeneous equations has a nontrivial solution when:

$$D(q_y^o, q_y^e) = 0, \quad (53)$$

with

$$\begin{aligned} D(q_y^o, q_y^e) \equiv & -(q_y^o)^4 - (q_y^o)^3 \alpha_y + (q_y^o)^2 (k_x^2 - k_z^2 \varepsilon_{\perp} - \varepsilon_{\perp} q_y^e \alpha_y) \\ & + q_y^o (k_x^2 \alpha_y + k_x^2 \varepsilon_{\perp} q_y^e - \varepsilon_{\perp} q_y^e \alpha_y^2) + k_x^2 \varepsilon_{\perp} \alpha_y^2 \\ & + \varepsilon_{\perp} q_y^e \alpha_y k_x^2. \end{aligned} \quad (54)$$

Expression (53) is the dispersion relation for such a hybrid mode.

#### IV. DISPERSION RELATIONS

In this section our main purpose is to gain deeper insight into the nature of those SPP modes which can propagate on a face of a uniaxial anisotropic dielectric film. This can be achieved by studying in detail the dispersion relations of the various modes. We use a simplified dielectric function, based on the electron shell model, first proposed by Dick and Overhauser<sup>18</sup> and later elaborated by several researchers.<sup>19–23</sup> In this model the relevant charge oscillations is considered as displacements of the center of gravity of the valence electronic shell with respect to the ion core, and the frequency and wave vector dependent dielectric tensor is calculated in the harmonic approximation for these displacements. The characteristic wavenumber of the excitations in the STEM-EEL spectroscopy under consideration is around  $\omega/v$ , which is about 10 nm (for electron beam velocities  $v/c=0.54–0.77$ , corresponding to 100–300-keV  $e$ -beam energies)]. Thus one can use the so called “local” ( $\mathbf{k}\rightarrow 0$ ), or “optical” dielectric function expressed in the principal crystallographic axes of the uniaxial crystal,  $\alpha = x, y, z$ , as

$$\varepsilon_{\alpha\alpha}(\omega) = 1 + \sum_{j=1}^{3n} \frac{\omega_{p,\alpha}^2(j)}{\omega_b^2(j) - \omega^2 - i\omega\Gamma_b(j)}, \quad (55)$$

where  $\omega_{p,\alpha}(j) = \omega_{p,\alpha}(\mathbf{k}\rightarrow 0, j)$  is the effective long wavelength plasmon frequency at the  $j$ -th electronic branch ( $j = 1, 2, \dots, 3n$ ;  $n$  is the number of atoms in a unit cell). There are  $3n$  electronic branches with bound frequencies  $\omega_b(j)$ , and the corresponding damping parameters are:  $\Gamma_b(j)$ .

Restricting ourselves to the low-lying electron branches, we further simplify the analysis by using only three oscillators. For the uniaxial medium studied here there are only two independent components for the dielectric tensor:  $\varepsilon_{zz} \equiv \varepsilon_{\parallel}$  and  $\varepsilon_{xx} = \varepsilon_{yy} \equiv \varepsilon_{\perp}$ . The anisotropy is introduced via the plasmon frequencies only, while the bound frequencies and the damping parameters are assumed to be the same for both components. The three-oscillator model dielectric tensor exploited in the calculation below [see Figs. 2 and 3(a)] provides a reasonable reproduction of the 2H-MoS<sub>2</sub> experimentally derived function.

Dispersion relations for the various SPP modes can be obtained now by solving Eqs. (35) and (36) under the additional constraints  $\alpha_z > 0$  and  $[q_z^e(\omega)]^2 > 0$ , which ensure that the electric field associated with the corresponding charge oscillations decays on both sides of the film face. In the limit where all the damping parameters  $\Gamma_b(j)$  vanish so that the dielectric functions are purely real both  $\alpha_z^2(\omega)$  and

$$[q_z^e(\omega)]^2 = (\varepsilon_{\perp}/\varepsilon_{\parallel})[\alpha_z^2(\omega) - (\omega/c)^2(\varepsilon_{\parallel} - 1)] \quad (56)$$

should be positive for all the SPP frequencies  $\omega$  located below the light line (LL),  $\omega = ck$  [or  $\alpha_z(\omega) = 0$ ].

To study the effect of anisotropy let us first consider the semi-infinite limit  $c^* \rightarrow \infty$ . In this case both Eqs. (35), and

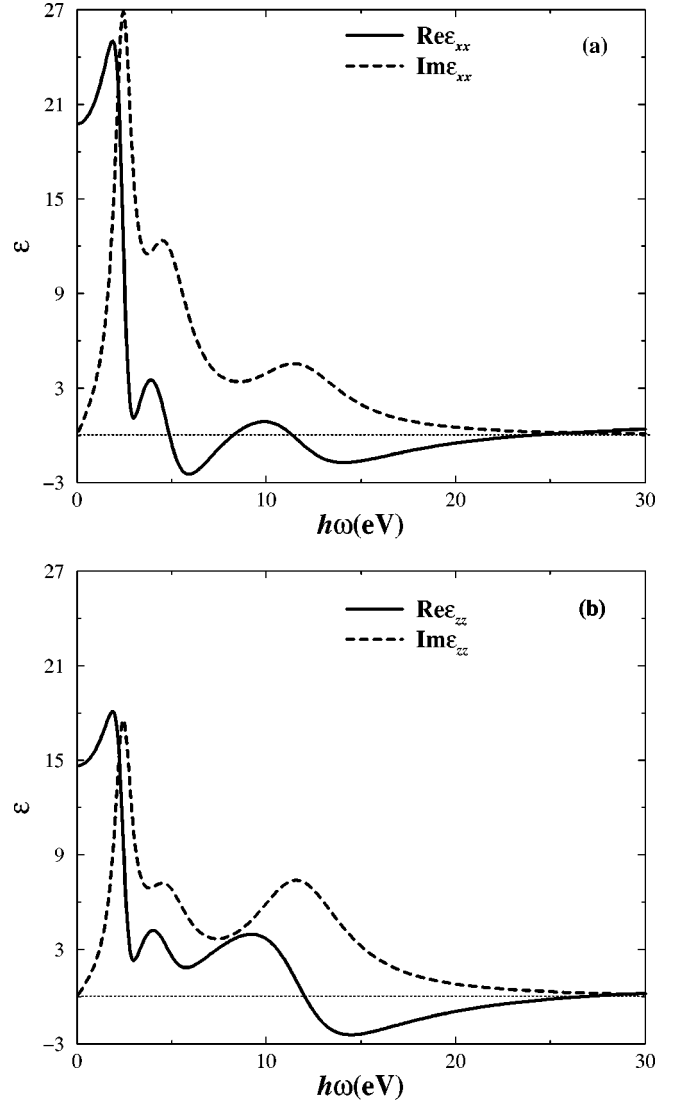


FIG. 2. Frequency dependent dielectric tensor representing a uniaxial anisotropic crystal in the electronic plasma oscillations region: (a)  $\varepsilon_{xx} \equiv \varepsilon_{\perp}$  and (b)  $\varepsilon_{zz} \equiv \varepsilon_{\parallel}$ . Calculations are according to the three-oscillator shell model [Eq. (55)] with oscillator parameters: bound frequencies  $\omega_b(1) \equiv \omega_1 = 2.5$  eV,  $\omega_2 = 4.9$  eV, and  $\omega_3 = 12$  eV and damping constants  $\Gamma_b(1) \equiv \Gamma_1 = 1.1$  eV,  $\Gamma_2 = 3.1$  eV, and  $\Gamma_3 = 6$  eV, plasma frequencies: (a)  $\omega_{p,x}(1) \equiv \omega_{x1} = 8$  eV,  $\omega_{x2} = 12.5$  eV, and  $\omega_{x3} = 17$  eV (b)  $\omega_{p,z}(1) \equiv \omega_{z1} = 6.5$  eV,  $\omega_{z2} = 9$  eV, and  $\omega_{z3} = 22.5$  eV. Note that the calculated dielectric functions resemble those derived experimentally for 2H-MoS<sub>2</sub>, reported in (Ref. 25).

(36) reduce to the equation  $\varepsilon_{\perp}\alpha_z + q_z^e = 0$ , which should be solved under the condition  $(q_z^e)^2 > 0$ . The solution for the extinction coefficient is:  $\alpha_z^2 = -(\omega/c)^2(\varepsilon_{\parallel} - 1)/(\varepsilon_{\perp}\varepsilon_{\parallel} - 1)$  and correspondingly  $(q_z^e)^2 = (\varepsilon_{\perp}\alpha_z^2)^2$ . The dispersion relations following from this solution,  $k^2 = (\omega/c)^2\varepsilon_{\parallel}(\varepsilon_{\perp} - 1)/(\varepsilon_{\parallel}\varepsilon_{\perp} - 1)$ , for our model dielectric tensor [Fig. 3(a)], are shown in Fig. 3(c). The corresponding dispersion relations for the isotropic case,  $\varepsilon_{\perp} = \varepsilon_{\parallel}$ , are shown in Fig. 3(b). The salient feature of the dispersion lines obtained in the anisotropic situation is the emergence of a split-off subband at the LL ( $\alpha_z = 0$ ) from each main band, except for the top

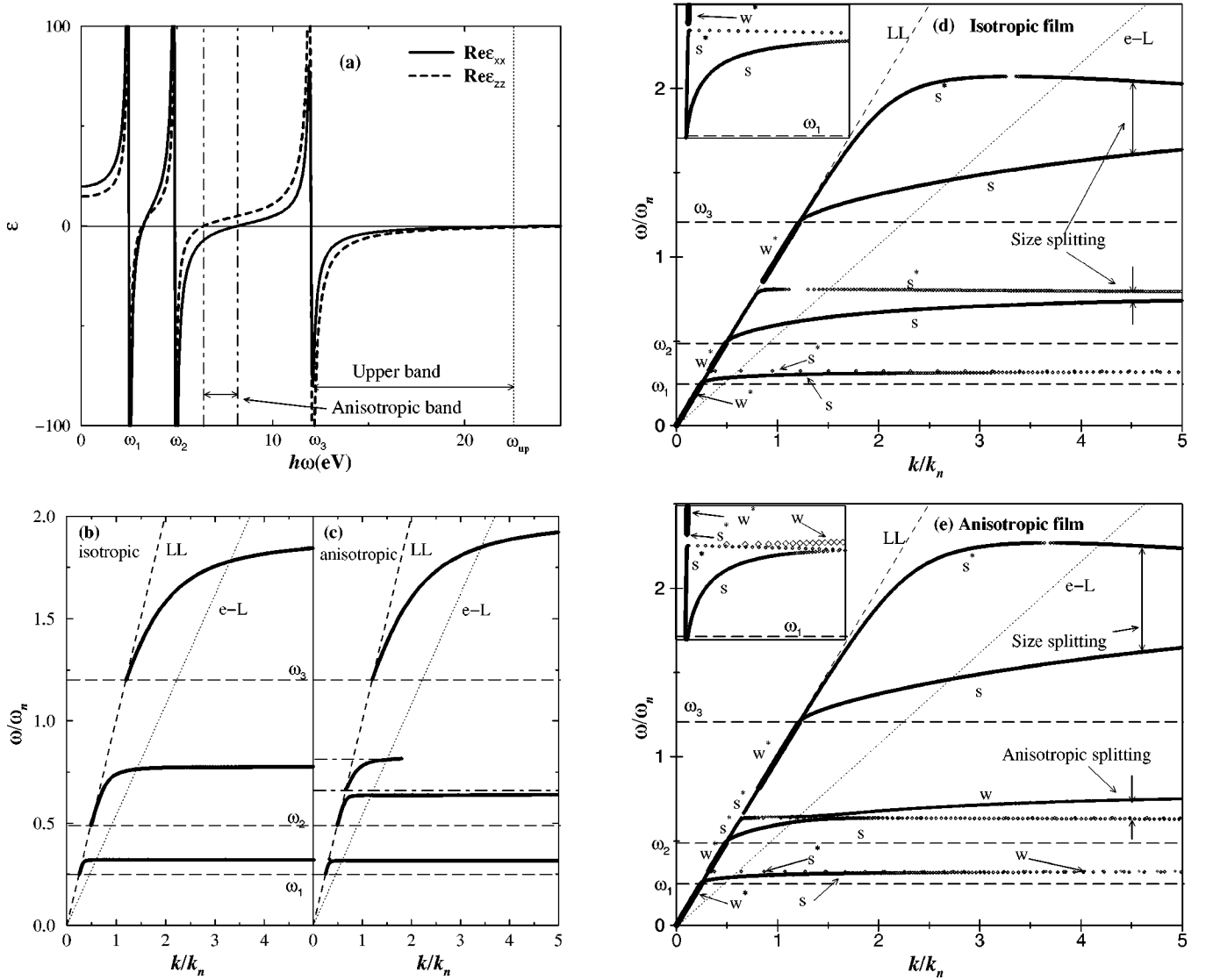


FIG. 3. Dispersion relations of nonradiative, symmetric ( $s^*, w^*$ ), and antisymmetric ( $s, w$ ) SPP and wave-guide modes, respectively, in uniaxially anisotropic dielectric film [with thickness  $2c^* = 40 \text{ \AA}$  (e)]. The dielectric tensor used in the calculations shown in (a) is identical to that presented in Fig. 2 with all damping parameters set equal to zero. Frequency and wave-number scales are given in units of  $\omega_n = 10 \text{ eV}$  and  $k_n = \omega_n/c$ , respectively;  $\omega_{up}$  in (a) corresponds to the maximum of the upper dispersion branch in (e). The corresponding dispersion lines in an isotropic film are shown in (d). The limiting case of a semi-infinite slab is shown in (b) and (c). Note that the bound frequencies  $\omega_{1,2,3}$ , shown by long-dashed lines, determine the lower edges of the SPP bands. Also note the emergence of a split-off subband from the main SPP band in (c), and the related anisotropic splittings in (e). The enlarged portion of the low-lying band is shown in the insets. The light line,  $\omega = ck$ , and the  $e$ -beam line,  $\omega = vk$  are indicated by LL and  $e$ -L respectively. Also note the continuous connection between SPP and wave-guide subbands within any branch belonging to a given symmetry.

one, at frequency  $\omega$ , where  $\varepsilon_{\parallel} = 1$ , corresponding to a zero of  $q_z^e$  [see Eq. (56)]. The subband terminates at a second zero of  $q_z^e$ , where  $\varepsilon_{\perp} = 0$ .

Returning to the finite slab, the long wavelength limit,  $q_z^e c^* \leq 1$ , turns out to be quite useful. Approximating  $\tanh x \approx x$ , and  $\coth x \approx 1/x + x/3$ , the solution of Eqs. (35) and (36) yields the following implicit forms of the dispersion relations:

$$k^2 = \left(\frac{\omega}{c}\right)^2 + [\alpha_z^{s,a}(\omega)]^2, \quad (57)$$

where

$$\alpha_z^s(\omega) = \frac{\varepsilon_{\parallel}}{2c^*} \left\{ -1 \pm \left[ 1 + \left(\frac{\omega}{c}\right)^2 \left(\frac{2}{\varepsilon_{\parallel}}\right)^2 (\varepsilon_{\parallel} - 1) \right]^{1/2} \right\} \quad (58)$$

is the solution for the extinction coefficient obtained from the symmetric branch of the dispersion relation [Eq. (35)] and

$$\alpha_z^a(\omega) = \frac{3\varepsilon_{\parallel}}{2c^*} \left\{ -1 \pm \left[ 1 + \left( \frac{\omega}{c} c^* \right)^2 \left( \frac{2}{3\varepsilon_{\parallel}} \right)^2 (\varepsilon_{\parallel} - 1) - \frac{4}{3\varepsilon_{\parallel}\varepsilon_{\perp}} \right]^{1/2} \right\} \quad (59)$$

is the extinction coefficient derived from the antisymmetric branch [Eq. (36)]. Note that the branch-point of the square-root in either Eq. (58) or (59) occurs at a maximum of the corresponding dispersion curve [see Figs. 3(d) and 3(e)].

We may now distinguish between essentially two different frequency regions, depending on the relative signs of  $\varepsilon_{\parallel}$  and  $\varepsilon_{\perp}$ , as explained below Eqs. (38) and (39).

In the first case, where both  $\varepsilon_{\perp}$  and  $\varepsilon_{\parallel}$  are negative, i.e.,  $\varepsilon_{\perp}/\varepsilon_{\parallel} > 0$ , the dispersion lines follow essentially the well known band structure of an isotropic medium, shown in Fig. 3(d), where bands of (symmetric and antisymmetric) waveguide modes appear in energy gaps of SPP modes. These guided-wave modes are always restricted to the close vicinity of the LL,  $\alpha_z = 0$ .

In the second case, where  $\varepsilon_{\perp}/\varepsilon_{\parallel} < 0$ , the anisotropy is essential, that is, the isotropic limit can not be approached without crossing a zero of either  $\varepsilon_{\perp}$  or  $\varepsilon_{\parallel}$ . As can be seen from Eqs. (56) and (59), in the frequency range where  $\varepsilon_{\parallel}(\omega) > 0$  and  $\varepsilon_{\perp}(\omega) < 0$  [in Fig. 3(a) see the anisotropic band], the wave-guide modes can exist at large  $k$ , away from the LL [see the wave-guide mode branches  $w$  in Fig. 3(e), corresponding to the antisymmetric branch of the dispersion relations, Eq. (36)]. These anisotropy-induced modes have strong polarization character and can be coupled effectively to the external electron via its exponential tail outside the film (see Sec. V).

All dispersion lines shown in Figs. 3 are restricted to the region lying below the LL,  $\alpha_z = 0$ , corresponding to nonradiative modes. Mathematically speaking, one may carry out an analytical continuation of the algebraic equation (57), into the region  $\alpha_z^2 < 0$ , which yields radiative modes, lying above the light-line in Fig. 3 (see Sec. V).

The SPP dispersion relations described above are of great importance because of the high (relativistic) velocity of the  $e$ -beam, which sets the scale of the electron-plasmon momentum transfer along the beam direction at  $k_x = \omega/v \sim \omega/c$ . This situation is illustrated in Fig. 3, where in addition to the LL,  $\omega = ck$ , the so called “ $e$ -beam line” ( $e$ -L),  $\omega = vk$ , is shown. The close proximity of these lines, typical to the experiments, implies that the excitation by the  $e$ -beam occurs at the strongly dispersive region of the SPP modes, their characteristic wavelength coinciding with the nanometer dimensions of the particle, thus providing enhanced sensitivity of the spectroscopy to particle geometry and size (see Sec. V).

## V. APPLICATION OF THE ELECTRODYNAMIC THEORY TO NEAR-FIELD EELS

The general EM theory, developed in the previous sections, can now be applied to a concrete physical situation of the energy loss processes probed by a converging STEM electron beam. It is customary to use for the corresponding

spectral loss function the standard expression (see, e.g., Ref. 14), derived under the assumptions that the path of the beam electron is classical and rigid (i.e., not affected by the interaction with the dielectric medium). These assumptions are clearly violated in some interesting cases (see below). Let us, for the sake of simplicity, ignore such quantum mechanical effects for a moment. Thus, within the framework of the classical approach, the total power loss  $\Delta W$  of the beam electron, moving along the  $x$  axis, which is assumed to be parallel to an infinite object face, is given by

$$\Delta W = e \int_{-\infty}^{\infty} v dt E_x[\mathbf{r}_e(t), t], \quad (60)$$

where  $\mathbf{r}_e(t) = (vt, 0, b)$  is the position vector defining the electron classical trajectory,  $v$  and  $(-e)$  are the electron velocity and charge respectively. The corresponding differential power loss, per unit path length per unit loss energy,  $d^2P/d\omega dx$ , is given by  $d\Delta W/dx = \int_0^{\infty} d\omega \hbar \omega (d^2P/d\omega dx)$ .<sup>14</sup>

We start with the situation when the symmetry axis  $z$  is perpendicular to the exposed platelet face. The current density associated with the  $e$  beam,

$$j_x(\mathbf{r}, t) = -ev \delta[z - (c^* + b)] \delta(y) \delta(x - vt), \quad (61)$$

corresponds to an electron propagated at a distance  $b$  (the impact parameter) above the nanoplatelet face  $z = c^*$  with velocity  $v$  along the  $x$  axis.

To apply the theory developed above for a finite rectangular platelet we restrict the beam position to the spatial region near a platelet face, and sufficiently far from its edges, where the influence of the corners can be neglected. Under these circumstances one may be allowed to use the separation of variables method employed in the implementation of the boundary conditions in Sec. III.

To find the component of the electric field,  $E_x(\mathbf{r}, t)$ , responsible for the power loss at the beam positions, we should now solve the system of equations for the coefficients  $A$  and  $B$  (obtained from the boundary conditions at  $z = \pm c^*$ ), which include the particular solution of inhomogeneous equations (8),

$$\Pi_x^{ext}(z, k_x, k_y, \omega) = \frac{\pi e v}{i \omega \varepsilon_0 \alpha_z} \delta(k_x v - \omega) \times \exp[-\alpha_z |z - (c^* + b)|], \quad (62)$$

associated with the current density [Eq. (61)]. The coefficients  $A_+$  and  $B_+$  are the only ones needed for the calculation of the loss function [Eq. (60)].

Combining Eqs. (18), (9), (16), and (51), and the calculated values of  $A_+$  and  $B_+$ , and substituting into Eq. (60), one obtains the following expression:

$$\frac{d^2 P^{(z)}}{d\omega dx} = \frac{e^2}{2\pi^2 \varepsilon_0 v^2 \hbar} \int_0^\infty dk_y \operatorname{Im} \left\{ \exp(-2\alpha_z b) \times \frac{\alpha_z}{k^2} \times \left[ 1 - \frac{k^2}{\alpha_z^2} \left( 1 - \frac{v^2}{c^2} \right) \right] \frac{\alpha_z^2 - q_z^{o2}}{2q_z^o \alpha_z \coth(2q_z^o c^*) + \alpha_z^2 + (q_z^o)^2} + \frac{(\varepsilon_\perp \alpha_z)^2 - q_z^{e2}}{2\varepsilon_\perp \alpha_z q_z^e \coth(2q_z^e c^*) + (\varepsilon_\perp \alpha_z)^2 + (q_z^e)^2} \right\}. \quad (63)$$

Note that in deriving this expression we have taken advantage of the time reversal symmetry of the dielectric response function, implying that the integrand is even in  $k_y$ , and that the dielectric tensor components satisfy  $\varepsilon_{ik}(-\omega) = \varepsilon_{ik}^*(\omega)$ . In the limiting case of a semi-infinite isotropic medium, Expression (63) coincides with that derived in Ref. 14. When each of the two denominators appearing in Eq. (63) vanishes there is a resonant contribution to the loss function corresponding to excitation of a collective EM mode by the  $e$  beam. The corresponding conditions coincide with the dispersion relations, Eqs. (33) and (34), and their separated appearance in Eq. (63) reflects the separability of the ordinary and extraordinary waves propagating along the surface normal to the symmetry axis. It should be noted, however, that only the  $e$  wave can satisfy the resonance condition for a surface mode (see the discussion in Sec. III).

A similar procedure, though more involved, yields for the valence electron excitation in a slab parallel to the symmetry axis, and an  $e$  beam corresponding to  $j_x(\mathbf{r}; t) = -ev \delta[y - (b^* + b)] \delta(z) \delta(x - vt)$ ,

$$\frac{d^2 P^{(y)}}{d\omega dx} = \frac{e^2}{2\pi^2 \varepsilon_0 \hbar v^2} \int_0^\infty dk_z \operatorname{Im} \left\{ \exp(-2\alpha_y b) \times \left[ - \left( 1 - \frac{v^2}{c^2} \right) \frac{A(q_y^o, q_y^e)}{\alpha_y D(q_y^o, q_y^e)} + \frac{2\alpha_y [q_y^{o2} - \varepsilon_\perp q_y^e q_y^o + k_x^2 (\varepsilon_\perp - 1)]}{D(q_y^o, q_y^e)} \right] \right\}, \quad (64)$$

where  $D(q_y^o, q_y^e)$  is determined by expression (54), and

$$A(q_y^o, q_y^e) = (q_y^o)^4 - (q_y^o)^3 \alpha_y + (q_y^o)^2 (-k_x^2 + k_x^2 \varepsilon_\perp + \varepsilon_\perp q_y^e \alpha_y) + q_y^o (k_x^2 \alpha_y - k_x^2 \varepsilon_\perp q_y^e - \varepsilon_\perp q_y^e \alpha_y^2) + k_x^2 \varepsilon_\perp \alpha_y^2 - \varepsilon_\perp q_y^e \alpha_y k_x^2. \quad (65)$$

In the special case of isotropic medium,  $q_y^o = q_y^e = q_y$ , in the nonrelativistic limit, Eq. (64) reduces to a well known expression<sup>14</sup>.

An interesting situation may be realized experimentally when the nanoplatelet dimension along one direction, say the  $z$  axis, is small compared to the characteristic wavelength  $c/v$ , and much smaller than along the other ones, such that  $b^* \gg c^*$ . Hence for the  $e$  beam in a  $z$ -scan configuration the boundary conditions at  $y = \pm b^*$  are not very important, and

the allowed values of  $k_y$  can be considered as quasicontinuous since  $\Delta k_y \sim 1/b^* \ll k_x$  even in the low energy region.

However, in a  $y$ -scan configuration, where the exposed platelet face has a small dimension (i.e., along the  $z$  axis), the boundary conditions at  $z = \pm c^*$  should be considered more carefully. These conditions stem from the continuity of  $E_y^o$  and  $H_x^o$  at  $z = \pm c^*$ , which yield, e.g., for the symmetric branch, the confinement condition

$$\tan k_z c^* = \frac{\sqrt{k_x^2 + l_y^{o2} - (\omega^2/c^2)}}{k_z}, \quad (66)$$

where  $l_y^o = \operatorname{Im} q_y^o = (\omega/\sqrt{2}c) \{ [\tilde{K}^4 + (\operatorname{Im} \varepsilon_\perp)^2]^{1/2} - \tilde{K}^2 \}^{1/2}$ , and  $\tilde{K}^2 \equiv (c/\omega)^2 (k_z^2 + k_x^2) - \operatorname{Re} \varepsilon_\perp$ . In the nonrelativistic limit,  $\tilde{K}^2 \gg 1$ , this condition reduces to  $\tan k_z c^* \approx \sqrt{k_x c^*} \approx \sqrt{(\omega/v)c^*}$ , which imposes quantization on the possible values of  $k_z$ . For a sufficiently thin film such that  $(\omega/v)c^* \ll 1$ , the smallest possible value of  $k_z$  is

$$k_{z, \min} \approx \frac{1}{c^*} \left( \frac{\omega}{v} c^* \right)^{1/2}.$$

This implies that the integral over  $k_z$  in Eq. (64) for the loss function in the  $y$ -scan configuration should be replaced by a discrete sum, starting with the minimal value  $k_{z, \min}$ . The resulting cutoff of the corresponding extinction coefficient  $\alpha_y$ , significantly alters the dependence of the loss function on  $b$  with respect to that obtained in the  $z$ -scan configuration<sup>24</sup> (see Sec. VI).

Applying the model dielectric function [Eq. (55)] (as specified in Fig. 2) to the above expressions for the loss function in both the  $z$ - and  $y$ -scan configurations, it is now possible to study in detail the  $b$  dependence of the EEL spectrum of nanoplatelets, which is capable of revealing various EM quantum size effects. For example, the development of the well known surface plasmon splitting, due to the interaction between two opposite faces of the platelet,<sup>6</sup> can be detected just by varying the impact parameter. The idea is illustrated in Fig. 4, by plotting the loss function of a thin platelet for values of the impact parameter  $b$ , varied through the value of the platelet thickness  $2c^*$ . The high energy broad band around 18 eV gradually splits into two resolved lines as  $b$  increases.

This dependence on the impact parameter  $b$  reflects a filtering effect in momentum space of the exponentially decaying factor  $e^{-2\alpha_z b}$ , which suppresses contributions of SPPs to the loss processes with wavelengths shorter than  $2b$ . Thus, for  $b < c^*$ , large values of  $k$ , at which the size splitting is significantly reduced [see Fig. 3(d)], dominate the loss function. For larger values of  $b$  only small values of  $k$ , for which the splitting is pronounced, contribute significantly to the loss function, thus resulting in larger splitting energy.

It should be noted that for many realistic materials the effect of the dielectric function anisotropy on the loss function in the energy range of interest here is not very important. This is mostly due to significant interband transitions, resulting in large damping parameters  $\Gamma_b(j)$ . To study the effect of this damping the loss function shown in Fig. 4(a) for

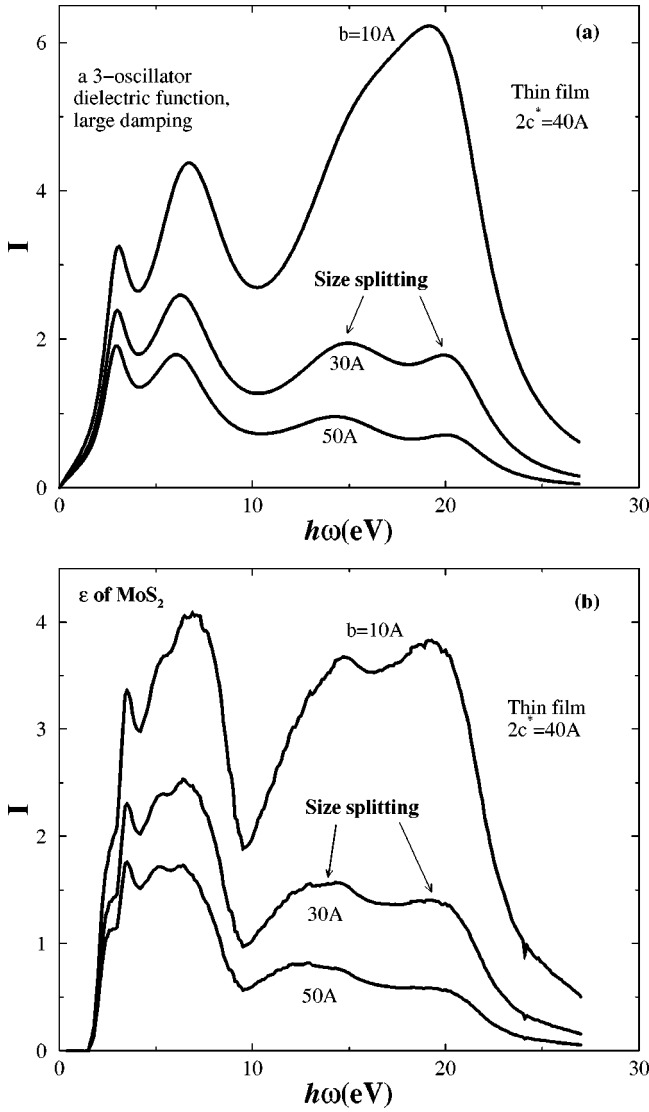


FIG. 4. The  $k$ -space filtering effect, demonstrated by the development of SPP splitting as a function of the impact parameter  $b$ , in the range where it is comparable to corresponding object dimensions (see the text). Calculated loss functions are based on (a) a three-oscillator dielectric function (see Fig. 2) and (b) optically derived dielectric function of 2H-MoS<sub>2</sub> (Ref. 25). The film thickness is  $2c^* = 40 \text{ \AA}$  and the beam electron velocity is  $v = 0.54c$ .

impact parameter  $b = 30 \text{ \AA}$  is recalculated for unrealistically small values of the damping parameters. As expected [see Fig. 5(a)], all major peaks in the loss function are correlated very well with the asymptotic (high density of states) sectors of the corresponding dispersion lines shown in Fig. 3(e). For a thicker film, where the finite size effects are suppressed, the anisotropy-induced split-off subband, discussed at the end of Sec. IV, is clearly seen, yet at small damping only, as shown in Fig. 5(b). For the realistic values of the damping parameters this splitting is practically washed out.

An important, qualitatively different, size effect arises from the platelet finite dimension along the  $e$ -beam direction ( $x$  axis; see Fig. 1). The delta function  $\delta(k_x v - \omega)$ , appearing in Eqs. (63), reflects the requirement of conservation of

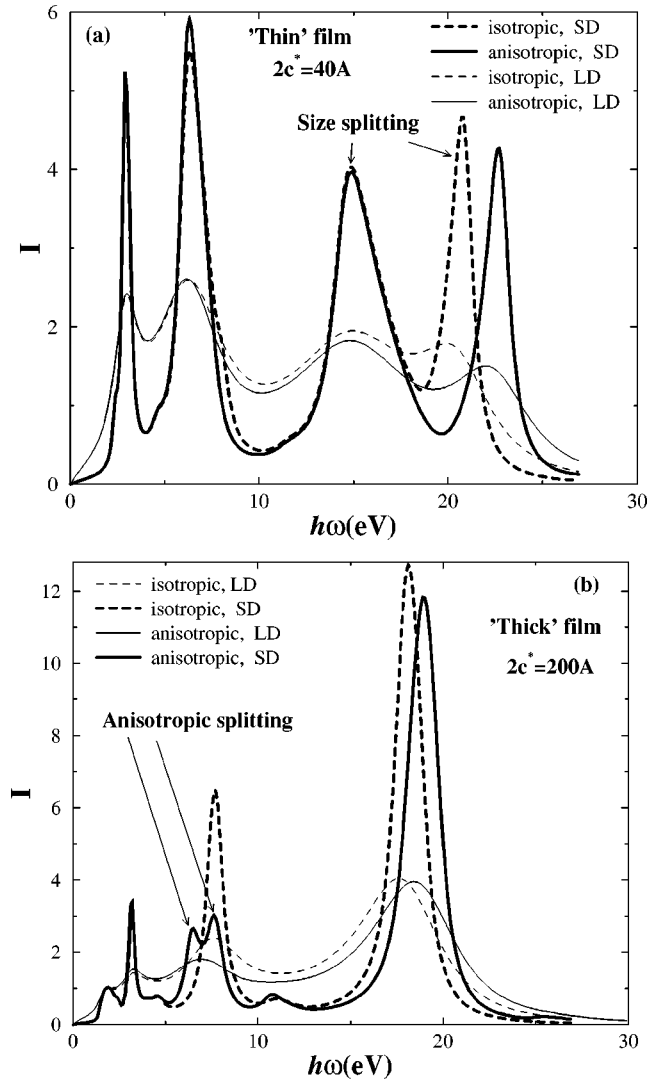


FIG. 5. Electron energy loss (EEL) in isotropic ( $\epsilon_{\parallel} = \epsilon_{\perp}$ ) and anisotropic ( $\epsilon_{\parallel} \neq \epsilon_{\perp}$ ) films with small and large damping parameters (indicated by SD and LD, respectively). In (a) the film thickness is  $2c^* = 40 \text{ \AA}$  and the only apparent effect of the anisotropy is in enhancing the finite-size splitting of the high energy SPP band [compare Figs. 3(d) and 3(e)]. In (b) the film thickness is  $2c^* = 200 \text{ \AA}$ , and the anisotropy leads to a significant splitting of the intermediate band, which is completely washed out by the large damping parameters. The other parameters are  $b = 30 \text{ \AA}$  and  $v/c = 0.54$ . The small damping (SD) situation was calculated with 25% of the large damping (LD) constants (used in Fig. 2). Note the remarkable correlation between peak positions and the high density of states ( $dk/d\omega$ ) regions in the dispersion lines shown in Fig. 3(e).

momentum along the beam direction in the electron-plasmon scattering. This constraint is inherent to the rigid classical trajectory model used above for the beam electron, which ignores the momentum uncertainty originating from the finite size of the target object. This effect can be introduced into the classical theory by replacing the strict delta function with a continuous distribution function of  $(k_x v - \omega)$ . The form of this distribution can be determined by comparing the classical expression for the loss function [Eq. (63)], to that derived

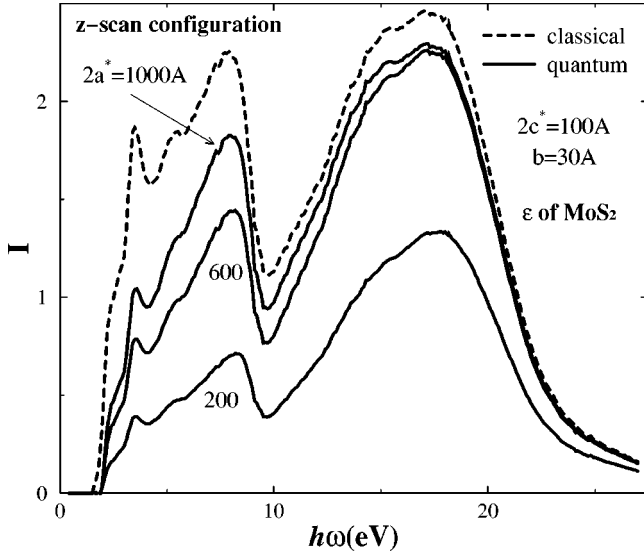


FIG. 6. Calculated loss functions for a 2H-MoS<sub>2</sub> nanoplatelet in a z-scan configuration, in which the condition of momentum conservation along the beam direction is relaxed due to the finite size of the platelet (see the text). Curves corresponding to four sizes are shown:  $2a^* = 200, 600, \text{ and } 1000 \text{ \AA}$ , and  $\infty$ . The other parameters used are  $2c^* = 100 \text{ \AA}$ ,  $v/c = 0.54$ , and  $b = 30 \text{ \AA}$ . The experimentally derived dielectric tensor of 2H-MoS<sub>2</sub> is used.

in Ref. 3 by means of a full quantum mechanical approach. Thus we write

$$\frac{d^2 P_{qu}}{d\omega dx} = \frac{a^*}{\pi} \int dk_x \{ \text{sinc}[(k_x - \omega/v)a^*] \}^2 \times \frac{d^2 P_{cl}(k_x)}{d\omega dx}, \quad (67)$$

where  $P_{cl}(k_x)$  is the classical expression, given by Eq. (63) and  $\text{sinc}(qa^*) \equiv (1/a^*) \int_{-a^*}^{a^*} \exp(iqx) dx = \sin(qa^*)/(qa^*)$ . Evidently, in the limit  $a^* \rightarrow \infty$ , the distribution  $(a^*/\pi) \text{sinc}^2(qa^*)$  tends to a delta function and Eq. (67) reduces to the classical result [Eq. (63)]. In Fig. 6 the influence of this quantum mechanical correction on the loss function is illustrated for the z-scan configuration of the  $e$  beam.

It is seen that the breakdown of the strict momentum conservation condition along the beam direction, as expressed by Eq. (67), suppresses the power loss of the  $e$  beam to excitations of internal degrees of freedom of the platelet, due to momentum transfer to the platelet as a whole. Evidently, the skeleton of this quantum smearing effect is recognized as a classical recoil effect. The reduction of the EEL intensity becomes particularly strong in the energy region near  $\omega \sim v/a^*$ , where the momentum smearing  $\Delta k_x \sim 1/a^*$  approaches the characteristic  $e$ -beam line momentum  $\omega/v$ . Thus, by varying the platelet size  $a^*$  the shape of the entire electron loss spectrum changes drastically as compared to the classical one. Note the substantial reduction of the EEL intensity in the low energy region even for films as thick as  $2a^* \geq 1000 \geq \text{\AA}$ , which reflects the long range nature of the electron-plasmon interaction at the low energy branches near the  $e$ -beam line (see Figs. 3).

Finally, it should be noted that for sufficiently small values of  $a^*$  there would be significant contributions to the

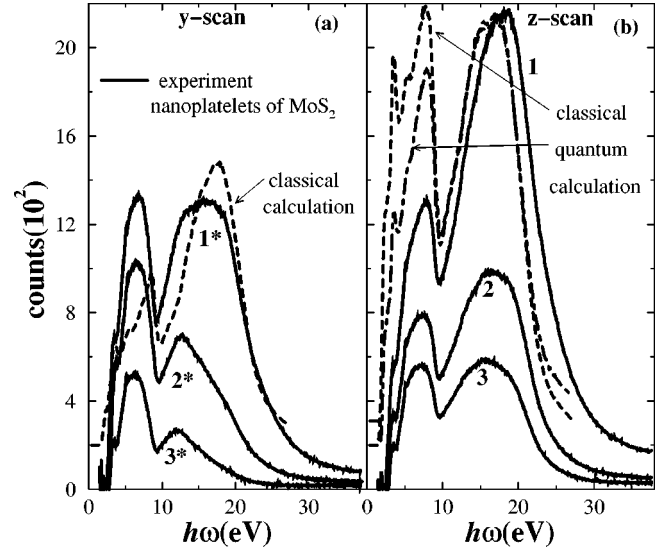


FIG. 7. Experimental near-field electron energy loss spectra of a 2H-MoS<sub>2</sub> nanoplatelet in z- and y-scan configurations. The impact parameter values are as follows: in the z-scan  $b = 36, 72, \text{ and } 108 \text{ \AA}$  for curves 1, 2, and 3, and in the y scan  $b = 25, 55, \text{ and } 85 \text{ \AA}$  for curves 1\*, 2\*, and 3\*, respectively. Calculated spectra (dashed curves) correspond to  $b = 36 \text{ \AA}$  in z and  $b = 25 \text{ \AA}$  in y (the other parameters:  $2c^* = 100 \text{ \AA}$  and  $v/c = 0.54$ ). The effect of the breakdown of momentum conservation along the beam axis due to the finite size of the object is illustrated by the dot-dashed curve. All calculated spectra are scaled by the same incoming beam flux parameter. An experimental dielectric function of 2H-MoS<sub>2</sub> (Ref. 25) is used in the calculations.

integral over  $k_x$  in Eq. (67), for which the values of  $\alpha_z$  were purely imaginary, and the SPP dispersion lines could penetrate beyond the light line. Under these conditions the  $e$  beam can be coupled to radiative modes of the platelet, which should be reflected in smoothly (nonexponentially) decaying dependence on the impact parameter. This striking situation requires a further study.

Experimental confirmation of the size effect discussed below Eq. (64) is shown in Fig. 7. The experimental data (see Ref. 3) for details) correspond to a MoS<sub>2</sub> rectangular platelet, ca  $100 \times 100 \times 10 \text{ nm}^3$  in size, and an  $e$  beam, propagating along  $x$  axis and progressively advancing along the  $z$  or  $y$  line scans. Spectra of representative pixels along the two line scans are shown, the z-scan advancing along the  $z$  axis towards the large platelet face and the  $y$  scan approaching the platelet narrow face along the  $y$  axis. Comparing  $y$ - and  $z$ -scan spectra, one may observe some minor spectral differences, yet the most striking observation concerns the line intensities, which show quite significant differences in decay rates. The high energy mode, for example, attenuates toward the  $y$  direction on a length scale about two times shorter than the corresponding  $z$ -scan attenuation.

Representative loss functions, calculated with Eqs. (63) and (64) [including the quantum correction, Eq. (67)], using an experimentally derived dielectric function<sup>25</sup>, are also presented in Figs. 7. In the z-scan configuration the calculated spectral features are in very good quantitative agreement with the corresponding experimental data. Given the ap-

proximate nature of the calculations, the comparison of the corresponding line intensities is rather good. It is stressed that only a single free parameter, the incoming beam flux, has been used here, kept with an identical value in all calculated spectra. In the  $y$ -scan configuration the agreement between theory and experiment (both in terms of line positions and intensities) deteriorates quickly as the impact parameter  $b$  increases (not shown). This finding is not well understood yet. It may arise from the complete neglect of the effect of the platelet corners in our calculation, which becomes a serious shortcoming in the  $y$ -scan configuration when the impact parameter becomes comparable to the narrow size  $c^*$ .

It is interesting to note that, similar to the experimental spectra, the calculated line scans differ substantially in their intensity decay as a function of the impact parameter  $b$ . Linear fits used to evaluate the effective attenuation parameters in both the calculated and experimental loss data, yield a directional ratio  $\alpha_y/\alpha_z$  of about 2. The origin of this effect is in the smaller size of the platelet along the  $z$  axis, and the strong quantization of the corresponding wave number  $k_z$ , as explained in the paragraph below Eq. (66). The minimal attenuation parameter along the  $z$  scan is  $\alpha_z^{\min}=(\omega/v)(1-\beta^2)^{1/2}$ , while  $\alpha_y^{\min}=(\omega/v)[v^2k_{z,\min}^2/\omega^2+(1-\beta^2)]^{1/2}\approx(\omega/v)\times[v/\omega c^*+(1-\beta^2)]^{1/2}$ . For typical values of the electron velocity  $v=0.54c$ , and the energy loss  $\hbar\omega=10$  eV in this experiment, we find the classical longitudinal wavelength  $k_x^{-1}=v/\omega\approx 100$  Å, so that for the platelet thickness  $c^*=50$  Å realized in the experiment, we find the theoretical estimate  $\alpha_y/\alpha_z\approx 1.95$ , in very good agreement with the experimentally derived value.

## VI. CONCLUSIONS

We have developed a theory for collective electromagnetic modes, which dominate the near-field regions outside thin films and nanoplatelets, taking into account the effect of medium anisotropy and finite dimensions of the platelet. Employing the electron shell model in a three oscillator approximation, a model dielectric tensor has been derived for the study of dispersion curves and excitation probabilities of the SPP and guided modes.

Our calculations show that hybridization of ordinary and extra-ordinary modes occurs on a surface of low symmetry, while complete separation takes place on surfaces perpen-

dicular to the symmetry axis. The extraordinary wave itself exhibits fine anisotropy splitting, which tend to easily smear as soon as large imaginary parts of the dielectric function are introduced, namely, with typically realistic values in the energy range of interband transitions. In contrast, it shows a great sensitivity to size and geometrical parameters at impact parameter values, which are comparable to corresponding object dimensions. Under certain conditions for the dielectric function components SPP modes transform into TE and TM guided modes.

The predicted sensitivity to size effects is due to a unique coincidence of all relevant length parameters in the STEM-EEL spectroscopy, and to the momentum space filtering imposed by the exponentially decaying electron-plasmon interaction in the vacuum, a value controlled by selecting the beam-nanoparticle impact parameter.

Two qualitatively different size effects could be distinguished. The first, relating particle finite dimensions in the plane perpendicular to the beam direction, strongly influences the intensity decay constants, thus resulting in directional sensitivity to the particle shape. The second effect is raised by the finite object size along the beam direction (and the corresponding breakdown of momentum conservation in the electron-plasmon scattering). This effect provides new channels of radiative plasmon excitations and results in drastic changes of the EEL pattern. An interesting interplay of relativistic and spatial dispersions has been shown to imply further effects on the spectral appearance of the surface modes.

Comparing our theory with experimental data of a semi-isolated MoS<sub>2</sub> nanoplatelet, a good quantitative agreement is obtained in the range of validity of our approximations. In particular, a strong EM quantum size effect is revealed by the dependence of the loss function on the impact parameter.

## ACKNOWLEDGMENTS

This research was supported by the BIKURA foundation of the Israel Academy of Science and Humanities and by the KAMEA foundation of the Center for Absorption in Science, Ministry of Immigrant Absorption, Israel and by the Association Franco-esraelienne pour la Recherche Scientifique et Technologique. We acknowledge C. Colliex and O. Stephan for kindly supplying us with the experimental data.

<sup>1</sup>A. Howie, *Ultramicroscopy* **11**, 141 (1983).

<sup>2</sup>P. M. Echenique, A. Howie, D. J. Wheatley, *Philos. Mag. B* **56**, 335 (1987).

<sup>3</sup>H. Cohen, T. Maniv, R. Tenne, Y. Rosenfeld Hacoheh, O. Stephan, and C. Colliex, *Phys. Rev. Lett.* **80**, 782 (1998).

<sup>4</sup>A. Howie and R. H. Milne, *Ultramicroscopy* **18**, 427 (1985).

<sup>5</sup>H. Raether, *Excitation of Plasmons and Interband Transitions by Electrons* (Springer, New York, 1980).

<sup>6</sup>H. Raether, *Surface Plasmons on Smooth and Rough Surfaces and on Gratings* (Springer, New York, 1988).

<sup>7</sup>L. D. Landau and E. M. Lifshitz, *Electrodynamics of Continuous*

*Media* (Pergamon Press, New York, 1960).

<sup>8</sup>A. A. Lucas, L. Henrard, and Ph. Lambin, *Phys. Rev. B* **49**, 2888 (1994).

<sup>9</sup>Ursula Schroter and Alain Dereux, *Phys. Rev. B* **64**, 125 420 (2001).

<sup>10</sup>L. Henrard, O. Stephan, and C. Colliex, *Synth. Met.* **103**, 2502 (1999).

<sup>11</sup>M. Kociak, L. Henrard, O. Stephan, K. Suenaga, and C. Colliex, *Phys. Rev. B* **61**, 13 936 (2000).

<sup>12</sup>O. Stephan, M. Kociak, L. Henrard, K. Suenaga, A. Gloter, M. Tence, E. Sandre, and C. Colliex, *J. Electron Spectrosc. Relat.*

- Phenom. **114-116**, 209 (2001).
- <sup>13</sup>M. Kociak, O. Stephan, L. Henrard, V. Charbois, A. Rothschild, R. Tenne, and C. Colliex, *Phys. Rev. Lett.* **87**, 075 501 (2001).
- <sup>14</sup>Z. I. Wang, *Micron* **27**, 265 (1996).
- <sup>15</sup>Simon Ramo, John R. Whinnery, and Theodore van Duzer, *Fields and Waves in Communication Electronics* (Wiley, New York, 1967).
- <sup>16</sup>W. L. Weeks, *Electromagnetic Theory for Engineering Applications* (Wiley, New York, 1964).
- <sup>17</sup>Amnon Yariv, *Optical Electronics in Modern Communications*, 5th ed. (Oxford University Press, New York, 1997).
- <sup>18</sup>B. G. Dick and A. W. Overhauser, *Phys. Rev.* **112**, 90 (1958).
- <sup>19</sup>A. D. B. Woods, W. Cochran, and B. N. Brockhouse, *Phys. Rev.* **119**, 980 (1960).
- <sup>20</sup>Lalit K. Banerjee and A. N. Basu, *Phys. Rev. B* **28**, 5730 (1983).
- <sup>21</sup>Y. R. Wang and A. W. Overhauser, *Phys. Rev. B* **35**, 497 (1987).
- <sup>22</sup>Y. R. Wang and A. W. Overhauser, *Phys. Rev. B* **35**, 501 (1987).
- <sup>23</sup>X. M. Chen and A. W. Overhauser, *Phys. Rev. B* **43**, 14 182 (1991).
- <sup>24</sup>H. Cohen, B. I. Lembrikov, M. A. Itskovsky, and T. Maniv (unpublished).
- <sup>25</sup>K. Zeppenfeld, *Opt. Commun.* **1**, 377 (1970).